Alignment of 3D woven textile composites towards their ideal configurations

Marcello Rubino, Arturo Mendoza, Yanneck Wielhorski, Keerthi Krishna Parvathaneni, Stéphane Roux

Alignment of 3D woven textile composites towards their ideal configurations

Marcello Rubino[a,b], Arturo Mendoza[a,c], Yanneck Wielhorski[b], Keerthi-Krishna Parvathaneni[a], Stéphane Roux[a,*]

[a] *Université Paris-Saclay/CentraleSupélec/ENS Paris-Saclay/CNRS, LMPS, 4, Avenue des Sciences, 91192 Gif-sur-Yvette, France*
[b] *Safran Aircraft Engines, Rond-point Réné Ravaud, 77550 Moissy-Cramayel, France*
[c] *Safran Tech, Rue des Jeunes Bois, 78772 Magny-les-Hameaux, France*

Abstract

The objective of the present study is to create a parametric model of an ideal 3D woven textile from a computed tomography at mesoscale without prior knowledge of the fabric architecture. The model is constructed by identifying a minimal number of parameters from the tomography and includes further assumptions about the textile properties (*e.g.*, equally-spaced vertical yarn columns). A novel registration procedure called Model-based Digital Image Correlation (MDIC) is introduced for mapping the whole textile image onto its own model. It leads to a realignment of the yarn columns after deforming the textile image, from which the model is updated. Model extraction and registration steps are iterated up to a stationary solution. The final result is a perfect textile geometry with straight and orthogonal yarn columns and its mapping onto the original tomography image. The proposed procedure is applied successfully to a 3D woven textile and a 3D-injected woven composite. This novel technique is useful as a pre-processing step to image segmentation procedures or to ease the visual inspection performed by operators in correcting the yarn paths and yarn column deformations occurring during composite material manufacturing. Additionally, this alignment procedure could be used to deform a numerical ideal model to better fit the geometry of a real weave.

Keywords: Digital Image Correlation, Computed Tomography, 3D Woven Composites

1. Introduction

Nowadays, the use of composite materials is soaring in industries where lightweight components are key. The aeronautic industry is a clear example of such. For example, the introduction of composite parts in the LEAP engine lead to an overall reduction of 15% of fuel consumption with respect to the

*Corresponding author.
Email address: stephane.roux@ens-paris-saclay.fr (Stéphane Roux)

best-performing engine of the previous generation [1]. In particular, the use of 3D woven technology for the fan blade and fan case was fundamental in its design. Moreover, the use of this textile architecture allows for optimizing the textile reinforcement so that its customized mechanical properties best respond to the operational loads and even complex net shapes such as the fan blade. For instance, 3D woven interlock fabrics, interlacing two-yarn types (warp and weft) along the thickness dimension, confer very interesting out-of-plane properties, hence reducing the risk of delamination.

In order to guarantee the final mechanical performances, non-destructive testing (NDT) techniques based on high-resolution X-ray computed tomography (micro-CT) images have proven to be extremely useful and suitable to composite materials [2]. Indeed, this allows non-destructive inspections of the actual arrangement of yarns within manufactured textiles (*i.e.*, just after weaving of the reinforcement and/or after matrix injection). From these CT images, visual inspection is performed through operators. Their role is, for example, to check the absence of missing yarns or anomalous yarn paths due to the weaving (*e.g.*, as could result from friction with the shuttle inserting weft yarns) or any misplacement of yarns. Even if very rare, these defects could be detrimental to the final mechanical performance and NDT is thus a crucial step in quality control. Moreover, these tomographic volumes allow to create digital material twins of fibrous reinforcements as well.

Indeed, many works devoted to extracting the mesoscale textile model, employ image processing techniques and perform quantitative analyses therein [3, 4, 5]. The techniques range from "classical" methods such as clustering operations [6] or texture analysis [7], up to the more recent Deep Learning approaches [8, 9, 10, 11, 12]. Other approaches based on deformable models have also been explored [13, 14]. The main idea is to start from a rough initial yarn path and a very coarse description of yarn shapes and to progressively deform the latter to fit them to the observed ones minimizing yarn interpenetration and adjusting yarn orientations, to name but a few.

So extracting the textile mesoscale model presents clearly many advantages to perform Finite Element Analyses on such complex structures. It could also be a pre-processing step to an automated control based on image analysis or machine learning. That being said, another strategy aiming at helping the aforementioned automated control (*e.g.*, , based on image analysis or machine learning) as a pre-processing step or simply easing the operator's visual inspection could also be explored.

Let z denote the thickness direction, while x and y correspond, respectively, to the warp and weft mean orientations. Weaving technology of 3D textiles leads to some generic constraints: warp yarns are structurally held in parallel planes (x, z), and weft yarns are also inserted in parallel planes

(y, z) orthogonal to the former. Thus, textiles are engineered through ideal models that obey these constraints so that the architecture describes how each yarn (weft or warp) navigates in the thickness direction. However, after manufacturing, the weave may be deformed and shaped to the final desired composite shape. Hence the initially parallel, equally spaced, orthogonal families of planes become distorted to curved and sheared surfaces. The fact that the weave has been deformed makes the visual inspection of CT images quite tricky, as one has to navigate in different cross-sections to follow each yarn individually. The present study aims to start from a CT volume and correct it so that warp and weft are "moved" back to their ideal configuration (that of the loom or the CAD model). The question is thus to find the geometrical transformation, $\mathcal{T}$, that will restore the perfect alignment of warp and weft planes. Because of its use for NDT purposes, the textile model is not assumed to be known in this work, so even if the topology is not obeyed strictly, it will not affect the transformation or its determination. Thus, the deliberate choice is not to segment individual yarns to reconstruct the deformed warp or weft planes. Instead, the large-scale structure will be considered, and the altered underlying warp and weft planes will guide our methodology for a robust approach. Such corrected CT images are thus much easier to control, limiting workload and the risk of misinterpretation. However, it is important to note that the proposed alignment is a deformation that affects the yarn cross-sections and fiber or yarn fractions. Those quantities are to be measured on the original CT volume. If needed, however, they can be mapped onto the ideal configuration, where a proper labeling of yarns for instance is naturally defined.

The above transformation also offers a side benefit. To assess the mechanical properties of the composite structure, it is usual to rely on finite element numerical simulation at the mesoscale. However, these simulations are often based on the CAD model of the textile in its *ideal* configuration. The mesh should be matched to the actual geometry to evaluate the effect of distortion or a defect (*e.g.*, a missing/broken yarn). This can easily be done using the inverse transformation, $\mathcal{T}^{-1}$ (now from the ideal geometry to the actual one).

As such, the aim of the present work is to develop a method based on the registration of "abstract" textile models for transforming the real images into *ideal* ones. Here, the abstract model aims to provide a simpler representation of the textile that conforms to an ideal configuration (*e.g.*, equally-spaced vertical yarn columns).

Since this method is based on measuring the relative deviations of a "known" real sample, in the form of a tomographic image, with respect to a numerical textile descriptor model, a registration method

such as Digital Image Correlation (DIC) (local [15] or global [16]), or Digital Volume Correlation (DVC) (here again local [17], or global[18, 19]) is well-suited. Previous works have shown the potential of such methods in the context of 3D-woven composites [20].

This study is presented as follows. Section 2 presents the studied tomographic samples (woven textile and composite part). Then, section 3 presents the chosen strategy for describing an ideal textile by incorporating some *a priori* (*e.g.*, perfectly aligned, orthogonal yarn columns, equal spacing between the columns). Afterward, section 4 details the proposed Model-based DIC (MDIC) by building up the problem from a 1D formulation up to a 3D solution. Finally, section 5 presents the results on both studied samples before concluding with some remarks and perspectives in section 6.

2. Tomography of 3D woven textiles

This section describes the two samples used for this study. The first one is a flat textile reinforcement (without a matrix), and the second one is a composite panel (with a resin matrix). Both samples are ply-to-ply angle interlocks (but with different weaving patterns) composed of carbon-fiber-based yarns.

Both samples were scanned with a GE Phoenix X-ray tomograph (GE v|tome|x L300) and an image resolution set to allow for a mesoscale analysis (*i.e.*, the yarns are distinguishable from each other, but the carbon fibers within them are not). Also, the samples are placed so that the warp columns are aligned with the x axis, the weft columns are oriented with the y axis, and the z axis corresponds to the textile thickness direction.

It should be noted that all calculations and computing times listed here been performed on an Intel i7 processor (4 cores) with 32 GB of RAM. Moreover, the code was developed using MATLAB.

2.1. Textile reinforcement sample

This first "dry" sample is shown in figure 1. It contains 39 warp yarns and 32 weft yarns (total of 71 yarns). The warp yarns are distributed alternately in a sequence of 4 and 3 yarns in two consecutive columns. Similarly, two consecutive weft columns are composed of 5 and 4 yarns respectively. In this sample, there are 11 warp columns and 7 weft columns. The chosen voxel size of 20 µm leads to a volume image of $1472 \times 1776 \times 408$ voxels.

This image is coarsened with an anisotropic downsampling with a ratio of 2:2:1 so that the yarns cross-sections are closer to a circular shape rather than elliptical. This was shown useful when analyzing

Figure 1: Reconstructed volume of the 3D woven fabric specimen.

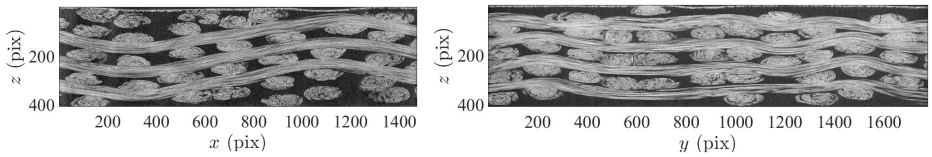

(a) Original volume (warp slice)

(b) Original volume (weft slice)

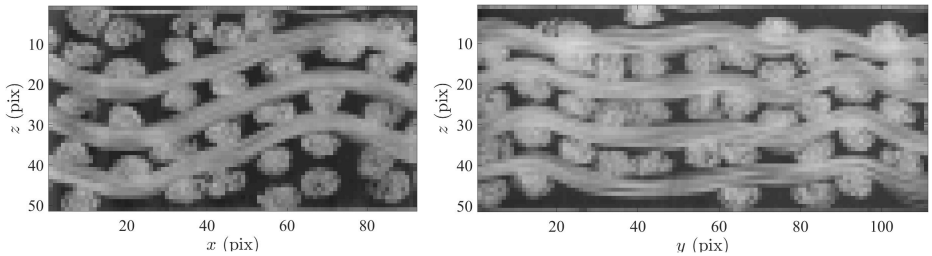

(c) Coarsened volume (warp slice)

(d) Coarsened volume (weft slice)

Figure 2: Visualization of mid x-z and mid y-z planes for both the original and coarsened volumes of the 3D woven fabric specimen. The indicated yarn types are seen longitudinally. The fine texture within the yarns is lost but the overall textile information is kept.

displacements of yarns [21] as similar displacement values along the two different in-plane directions will not have the same influence on the overall textile architecture. Afterwards, an isotropic downsampling by a factor 8 helps condensating the image so that only the *useful* features are maintained (*i.e.*, yarn boundaries are kept, while fiber definition is lost). Thus, the size of the obtained coarsened volume is $92 \times 111 \times 51$ voxels, with a final resolution of $320 \times 320 \times 160$ µm.

The two vertical mid-planes (for warp and the weft directions) are shown in figure 2 for the original and the coarsened volumes.

2.2. Flat composite sample

This second sample contains around 180 yarns distributed over warp and weft columns that are much closer between themselves than in the previous sample. It was scanned at a resolution of 42 µm

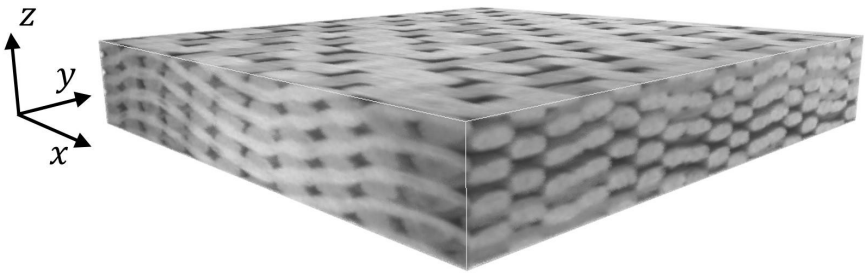

Figure 3: Reconstructed volume of the injected specimen

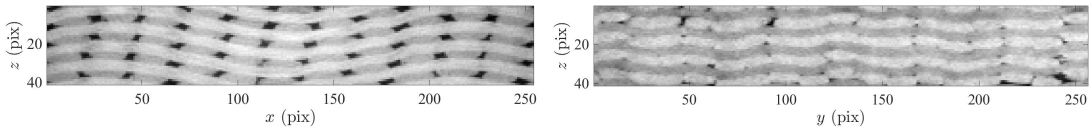

(a) Original volume (warp slice)

(b) Original volume (weft slice)

Figure 4: Visualization of mid x-z and mid y-z planes for the volume of the injected specimen. The indicated yarn types are seen longitudinally.

(voxel size). An isotropic downsampling was performed so that the resulting volume would have a similar final voxel size as the previous sample in x and y directions, resulting in a volume image of $254 \times 256 \times 41$ voxels (*i.e.*, 320 µm). It should be noted that in this case, the anisotropic scaling was found to be less favorable to the calculations. Given that this step merely acts as a numerical trick to speed-up the calculations, the results shown for this sample will keep its original aspect ratio. Figure 3 shows a 3D visualization of the coarsened volume, and figure 4 shows the two vertical mid-planes representing both warp and weft orientations.

3. Textile models

This section introduces the parametric textile model that will be used thoroughly in all the text. It is designed to describe an idealized textile and the actual one observed in the tomographic volume.

It should be noted that the textile model used here is essentially of 2D nature. As such, it does not seek to describe the exact position of every yarn on every textile layer but rather the average position of multiple yarns in their respective columns. Thus, the proposed processing pipeline adapts a single 2D model for an averaged representation of the 3D woven textile. Then, the same 2D model is adapted for every layer of the 3D woven composite, with the additional advantage to enforce regularity between layers.

As such, the first part of this section will focus on some preprocessing steps on the tomographic volume to ease a simple two-dimensional treatment of the textile. Next, the "building blocks" for the parametric model will be described. They hinge upon simple 1D functions defined over the 2D space. Finally, details are given for a simple identification procedure to construct the base textile model. As evoked earlier, this single model is meant to be adapted either to a 2D representation of the textile as well as to all of its layers. In such a case, the identification procedure is performed only once.

3.1. Preprocessing of the tomographic volume

The first type of transformation applied to tomographic volume $V_{ct}(x, y, z)$ is represented by a z-average operation which can be carried out to "summarize" the overall textile information (from 3D volume to a 2D image). The resulting image $I_z(x, y)$ represents the global averaged position of the yarn columns, which can be obtained by:

$$I_z(x, y) = \frac{1}{N_z} \sum_{z=1}^{N_z} V_{ct}(x, y, z) \tag{1}$$

where N_z denotes the number of voxels along the thickness.

In an ideal case, where yarn columns would be perfectly aligned with z and yarn orientations perfectly orthogonal, as shown in figure 5a, the resulting image $I_z^{ideal}(x, y)$ (see figure 5c) would be a grid of projected yarn columns as thick "stripes" whose intensities would indicate the number of yarns per column. However, from the actual image shown in figure 5b, the z-averaged image $I_z(x, y)$ (see figure 5d) presents distorted and non-uniform stripes. This is due to local yarn distortions, uneven distances between yarn columns, non-perfectly vertical columns, non-perfectly orthogonal yarn orientations, and even image aberrations due to tomographic artifacts (*e.g.*, cone artifact).

Next, in order to isolate just one yarn orientation, a blurring operation, consisting of a convolution with a 2D Gaussian kernel $G(l_x, l_y)$ of width l_x and l_y respectively along x and y axes, is applied to $I_z(x, y)$. Let us introduce λ_x and λ_y respectively as the average distance (expressed in voxels) between weft and warp yarn columns. In order to separate warp yarn columns, the chosen kernel is $G(\lambda_x, 0)$, while in case of weft yarn columns, the kernel would be $G(0, \lambda_y)$.

These preprocessing operations can be written as

$$I_{z,warp}(x, y) = G(\lambda_x, 0) \circledast I_z(x, y) \tag{2}$$

$$I_{z,weft}(x, y) = G(0, \lambda_y) \circledast I_z(x, y) \tag{3}$$

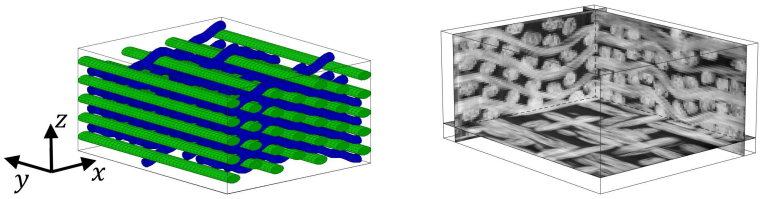

(a) Ideal textile

(b) $V_{ct}(x, y, z)$

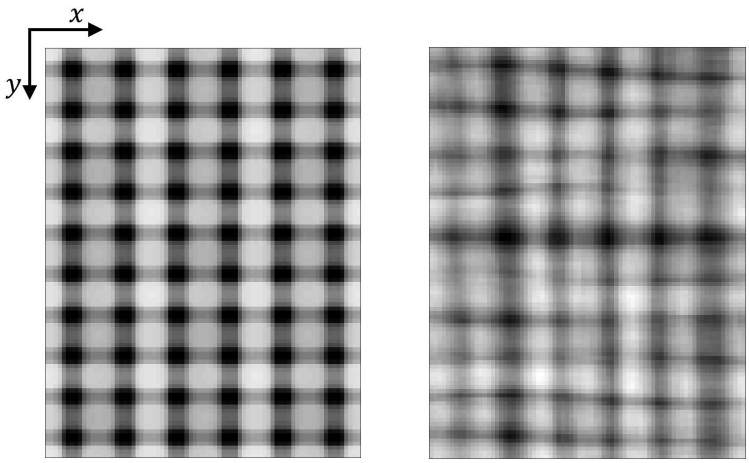

(c) $I_z^{ideal}(x, y)$

(d) $I_z(x, y)$

Figure 5: 3D textile image: top row (a) and (b) the 3D volume images; bottow row (c) and (d) the z-averaged projections

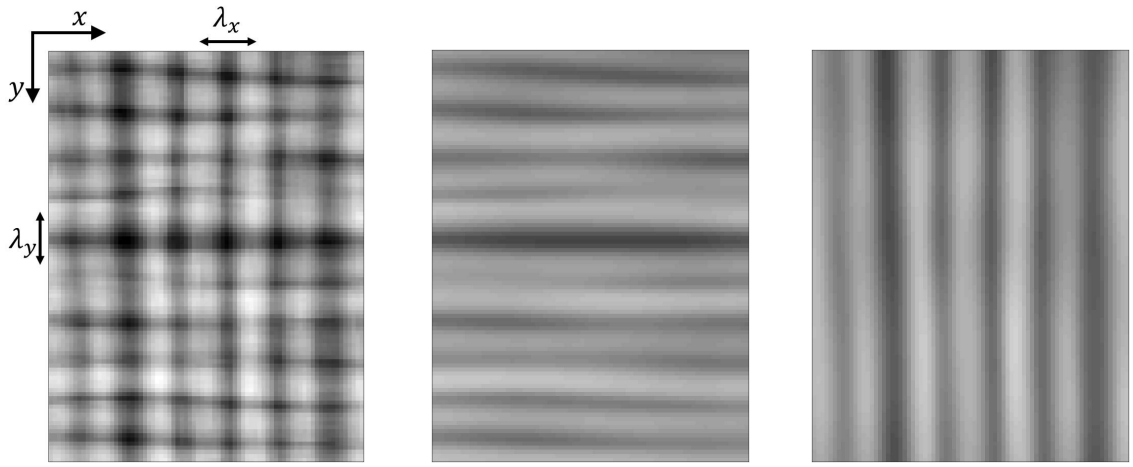

(a) $I_z(x, y)$ (b) $I_{z,warp}(x, y)$ (c) $I_{z,weft}(x, y)$

Figure 6: 2D Gaussian blurring: (a) raw image (in red the mean yarn column distances λ_x and λ_y); (b) and (c) the blurred images showing respectively only the warp and the weft yarn columns as continuous stripes.

where $\circledast$ denotes a convolution product.

It should be noted that λ_x and λ_y could be identified either by visual inspection (as it can be seen on figure 6a) or via numerical means (as mentioned in section 3.3). As a result, the obtained images $I_{z,warp}(x, y)$ and $I_{z,weft}(x, y)$, which are shown in figures 6b and 6c, depict a continuous evolution either for warp or weft yarn columns in the x-y plane without any discontinuities or holes.

Finally, for convenience, let us define a `Z_MEAN` function that computes the z-average $I_z(x, y)$ of the input volume $V_{ct}(x, y, z)$, and a `GAUSSIAN_BLUR` function that operates on $I_z(x, y)$ to compute $I_{z,warp}(x, y)$, $I_{z,weft}(x, y)$.

3.2. Construction of the parametric model

The proposed parametric model is built based on the tomographic image of the textile (*e.g.*, background gray level, or average yarn column spacing), and some assumptions about its characteristics (*e.g.*, yarn sizes). It should be underlined that such assumptions do not represent a prior knowledge of the full textile description or initial design, but rather a set of "common-sense" textile features easily measured in the image which will be tailored in this work to 3D woven ply-to-ply angle interlocks. These assumptions are depicted in figure 5a and can be summarized as:

- Yarn columns are mostly vertical (*i.e.*, roughly aligned with the z axis).
- Yarns undulate on their respective vertical planes and do not steer-off horizontally: warp yarns remain in their corresponding x-z planes, while weft yarns remain in their corresponding y-z

planes.

- Yarn columns are roughly equidistant and sufficiently separated.
- The warp and weft orientations are overall aligned with the x and y axes respectively (*i.e.*, orthogonality of yarn orientations).
- Yarns are continuous all along the observed sample (no cuts or missing segments).

First, a single parametric model $I^M(x, y)$ that describes the yarn column positions can be applied to $I_z(x, y)$. Second, the orthogonality of warp and weft yarns can be taken into account for isolating their contributions. As such, the model can be defined as:

$$I^M(x, y) = c_0 + I^M_{warp}(y) + I^M_{weft}(x) \tag{4}$$

with $I^M_{warp}(y)$ and $I^M_{weft}(x)$ as two one-dimensional functions that represent the ideal dispositions of warp columns on y, and weft columns on x, and c_0 is a constant used to account for the arbitrary gray level background used during the tomographic reconstruction.

Third, given that yarn columns are meant to be sufficiently separated, each one-dimensional signal can be modeled using a series of Gaussian profiles. Let us introduce the following notation

$$\mathbb{G}(x;\ c_1, c_2, c_3) = c_1 \exp\left(-\frac{(x - c_2)^2}{2c_3^2}\right) \tag{5}$$

defining the elementary Gaussian profile defined by its maximum intensity value c_1, its (central) position c_2, and its width c_3.

Warp and weft column distributions are hence described by a series of Gaussian profiles as follows:

$$I^M_{warp}(y) = \sum_{m=1}^{n_{cwarp}} \mathbb{G}(y;\ \beta_m, y_m, \omega) \tag{6}$$

$$I^M_{weft}(x) = \sum_{l=1}^{n_{cweft}} \mathbb{G}(x;\ \alpha_l, x_l, \omega) \tag{7}$$

Here, $I^M_{warp}(y)$ and $I^M_{weft}(x)$ are respectively composed of n_{cwarp} and n_{cweft} yarn columns. The peak intensities, $\{\beta_m\}$ and $\{\alpha_l\}$, as well as the peak positions, $\{y_m\}$ and $\{x_l\}$, are unique for each Gaussian profile (for $m \in [1, n_{cwarp}]$ and $l \in [1, n_{cweft}]$).. A single profile width ω is used for both warp and weft yarn columns because the yarn sizes are identical. In conclusion $2 + 2n_{cwarp} + 2n_{cweft}$ parameters need to be identified.

It is worth noting that more complex functions could be used for describing the yarn column profiles (at the cost of additional parameters). For instance, higher power exponential functions could be used here instead of Gaussian profiles in order to better describe a flattened shape for the peaks. Similarly, polynomial functions could be used to better capture possible inhomogeneous background intensity (instead of a constant value).

3.3. Identification of the parametric model

Let us first define the parametric model using the z-averaged information. Instead of performing a single identification on the $I_z(x, y)$ image, we propose to exploit the respective x and y-average of $I_z(x, y)$ (from 2D image to 1D signals), defined as follows:

$$I_{warp}^{ref,id}(y) = \frac{1}{N_x} \sum_{x=1}^{N_x} I_z(x, y) \tag{8}$$

$$I_{weft}^{ref,id}(x) = \frac{1}{N_y} \sum_{y=1}^{N_y} I_z(x, y) \tag{9}$$

where N_x and N_y respectively representing the image size along the x and y directions. Both strategies are equivalent but require different implementations.

As such, n_{cwarp} and n_{cweft} are identified using a peak detection algorithm on $I_{warp}^{ref,id}(y)$ and $I_{weft}^{ref,id}(x)$ respectively. At this stage, a first estimation of the distance between two consecutive peaks is provided as follows:

$$\Delta y_m = y_{m+1} - y_m \tag{10}$$

$$\Delta x_l = x_{l+1} - x_l \tag{11}$$

As well for the model, their mean values can be used to define λ_x and λ_y which will also use for the blurring operations. As such, for the dry textile sample, $\lambda_x = 13$ and $\lambda_y = 10$ were found.

Next, the peak positions and intensities are further refined using least squares regression on each cross-average image

$$\beta_m, y_m = \arg\min \| I_{warp}^{M}(y) - I_{warp}^{ref,id}(y) \|_2 \tag{12}$$

$$\alpha_l, x_l = \arg\min \| I_{weft}^{M}(x) - I_{weft}^{ref,id}(x) \|_2 \tag{13}$$

While the average width and background intensity are adjusted from the global model $I^M(x, y)$. This regression step is necessary since the detected peaks may not correspond to the overall best position for the Gaussian profiles.

Finally, for convenience, let us define a `GET_MODEL` function that solves equations (12) and (13) on $I_z(x, y)$ and returns $I^M(x, y)$, $I^M_{warp}(x, y)$, $I^M_{weft}(x, y)$ as defined in equations (4), (6) and (7).

4. Model-based Digital Image Correlation (MDIC)

The proposed correlation (DIC) algorithm is applied between a given image (*i.e.*, the real textile) and a model that has to be created starting from the same image but incorporating some assumptions about the weaving. As such, it represents an original extension of DIC called Model-based DIC (MDIC).

As presented beforehand, the first step of the proposed method consists of constructing a model image from the observed textile, based on its tomographic image. Next, a correlation should be performed between this model image and the tomographic one to estimate the displacement field that better registers them. Then, the inverse of the found displacement field is applied on the tomographic image so as to "align" the textile. This new image is used to re-adapt (*i.e.*, to correct) the parametric model and this registration procedure is repeated as many times as needed for convergence (overall correction displacement field close to zero). Each iteration of the whole procedure is called "great MDIC iteration".

This process can be carried out as a 2D problem or as 2 independent 1D problems. In the former case, the model aligns both yarn orientations simultaneously. In the latter case, each calculation identifies the displacement orthogonal to the analyzed yarn orientation.

As the distortions present along the textile thickness are not corrected by a simple 2D algorithm, the z invariance of the method is successively relaxed and the proposed MDIC algorithm is illustrated in its 3D version for re-aligning the entire textile volume.

This section will first recall the basis of DIC. Then, the full MDIC method will progressively be detailed.

4.1. Classical DIC

This section presents the principles of Digital Image Correlation (DIC) [22, 23, 24] for the registration of image pairs. DIC is based on the assumption of conservation of the gray level and aims to

find the displacement field $u(x)$ that best aligns (registers) a given image $g(x)$ onto a reference one $f(x)$ [25] by minimizing the L_2 norm of their *residual*:

$$\rho(x) = \tilde{g}(x) - f(x) \tag{14}$$

with the *corrected* image is defined as

$$\tilde{g}(x) = g(x + u(x)) \tag{15}$$

and the displacement field $u(x)$ that is discretized using a set of shape functions $\psi_i(x)$ inspired from the FE method [16, 26]. Then, an iterative Newton-Raphson algorithm is used to solve a linear version of the problem as:

$$[M]\{\delta u\} = \{b\} \tag{16}$$

with:

$$M_{ij} = \sum_{x \in \Omega} S_i(x) S_j(x) \tag{17}$$

$$b_i = \sum_{x \in \Omega} S_i(x) \rho(x) \tag{18}$$

where Ω corresponds to the region of interest, and the sensitivity fields $S_i(x)$ are commonly computed as

$$\begin{aligned} S_i(x) &= \nabla \tilde{g}(x) \cdot \psi_i(x) \\ &\approx \nabla f(x) \cdot \psi_i(x) \end{aligned} \tag{19}$$

It should be noted that the latter approximation is frequently used in DIC implementations since $\nabla \tilde{g}(x)$ approximates $\nabla f(x)$ at convergence. As a consequence, the matrix $[M]$ needs to be computed only once (as $f(x)$ does not change).

Finally, the displacement field at a given iteration k is updated with:

$$\{u\}^{(k+1)} = \{u\}^{(k)} + \{\delta u\} \tag{20}$$

This process is carried out until convergence or a maximum number of iterations is attained.

4.2. 1D-MDIC formulation

The 1D-signal model is constructed using the sum of Gaussian profiles as defined equations (6) and (7), for which, during the registration, the positions of the warp columns $y_m(x) = y_m^0 + u_m^y(x)$ depend only on x, while the positions of weft columns $x_l(y) = x_l^0 + u_l^x(y)$ depend only on y. Since for each yarn column, the correction to obtain is in the cross direction to the yarn longitudinal one, a two-dimensional image is required. As such, for the correction of weft yarns, the Gaussian model $g = I_{weft}^M(x)$ is spread along the yarn longitudinal direction y.

There are two main advantages of such a model. First, it involves displacements u, identified by 1D-MDIC, of each 1D-Gaussian profile with respect to an initial position. The second advantage is, paradoxically, the non-conservation of gray levels. Indeed, by definition, gray levels between Gaussian profiles increase when yarns become closer to each other or decrease if they get farther apart. This is in contrast with the usual assumption of DIC that would keep and stretch the initial gray values in between, but this is in agreement with a more realistic yarn transformation.

In summary, $g(x, y)$ can handle the model kinematics by a mere translation of the Gaussian profiles while also allowing for the proper conservation of X-ray attenuation (displacement has an impact on gray levels). Then, in the case of wefts, the corrected image, labeled as $\tilde{g}_{weft}(x, y)$, is written as

$$\tilde{g}_{weft}(x, y) = \sum_{l=1}^{n_{cweft}} \mathbb{G}(x;\, \alpha_l, x_l^0 + u_l^x(y), \omega) \tag{21}$$

This summarizing image is fundamental for computing the new sensitivity fields

$$\begin{aligned} S_l(x, y) &= \frac{\partial}{\partial u_l^x(y)} \tilde{g}_{weft}(x, y) \\ &= \frac{\partial}{\partial u_l^x(y)} \mathbb{G}(x;\, \alpha_l, x_l^0 + u_l^x(y), \omega) \\ &= \alpha_l \frac{(x - x_l^0 - u_l^x(y))}{\omega^2} \exp\left(-\frac{(x - x_l^0 - u_l^x(y))^2}{2\omega^2}\right) \end{aligned} \tag{22}$$

whose horizontal lines are used in equations (17) and (18) for the minimization problem. It should be noted that in the case of warp columns, the same kind of equations take place but with inverted axes and indices (*i.e.*, β and m instead of α and l).

Figure 7 shows an example of the 1D-MDIC algorithm on the top line of figure 6c and the model image $g(x) = I_{weft}^M(x)$ defined in equation (7).

Finally, let us explain how to extend the 1D-MDIC formulation so that it can be applied to 2D

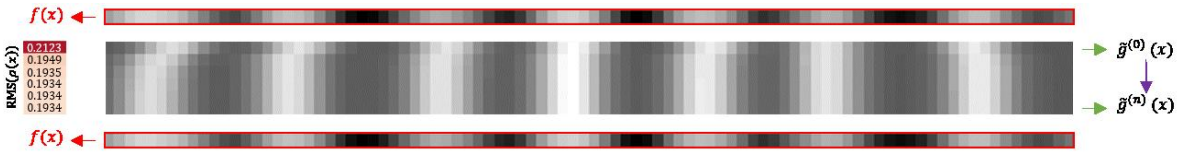

Figure 7: Example of 1D-MDIC algorithm where each line represents a signal (gray value as intensity). The reference $f(x)$ is indicated above and below the $\tilde{g}(x)$ block in which its evolution is shown for $n = 6$ iterations that lead to convergence. The evolution of the root mean square of the residuals (normalized with respect to the image dynamic range) is shown on the left.

images. The first "dense" strategy consists in performing 1D-MDIC computations in each line along the main column direction in the 2D images. However, as it was pointed out in the previous section, the pre-processing steps (namely blurring along x and y orientations) enforce a continuity between successive lines. So, the idea is to compute 1D-MIC only at the cross position of the in-plane orthogonal direction. So only n_{cweft} calculations are performed for $I_{z,warp}(x, y)$, while only n_{cwarp} calculations are performed for $I_{z,weft}(x, y)$.

Moreover, in order to obtain a complete displacement field over the 2D space of the image, simple interpolation can be used. Here, the same FE framework is employed as in classical DIC, and the resulting displacement field is expressed over a structured mesh with nodes at every yarn column crossing point. It is noteworthy that this latter strategy is considerably faster than the former (dense one) and avoids regularization issues as well.

An example using these two strategies is shown in figure 8 (using figure 6c as the reference image) at which a registration along x is carried out. The results obtained from both methods are essentially identical: the final disposition of yarn profiles (oriented along the second column), their final residual maps (oriented along the third column) and the obtained displacement fields (oriented along the fourth column), are almost coincident. In other words, the difference maps present very low values both in terms of normalized gray level and displacement. Moreover, note that, since both cases share a common reference image (see figure 8a), $\Delta\tilde{g} = \Delta\rho^f$.

Even if, in this case (the dry textile), the computational time is very fast, the dense approach is 10 times slower than the interpolated one (1.1 seconds vs 0.10 seconds, respectively), due to the very different number of registrations. For these reasons, the interpolated strategy is chosen for all further calculations and a `1D_MDIC`$(f(x, y), g(x, y))$ function is defined.

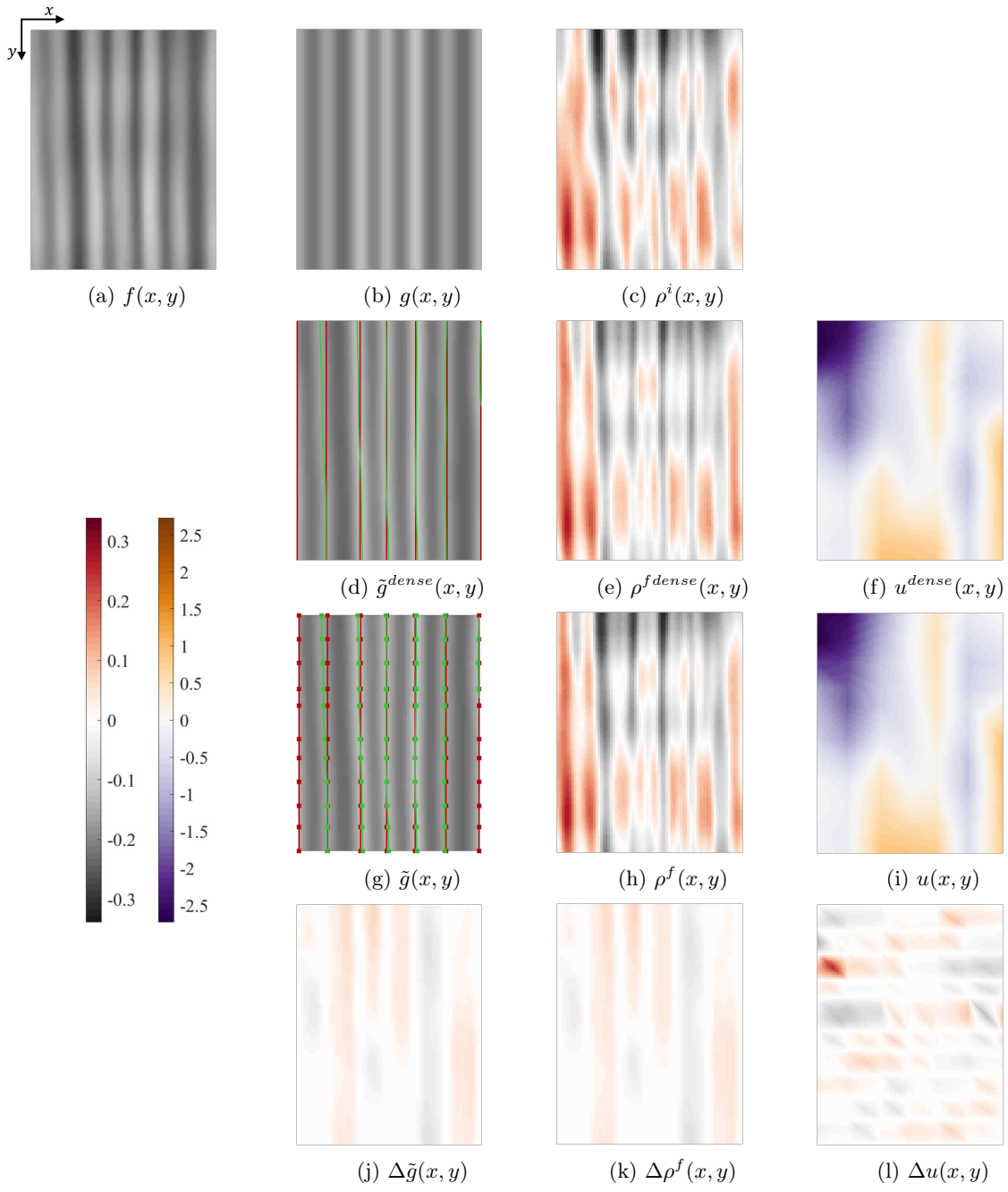

(a) $f(x,y)$ (b) $g(x,y)$ (c) $\rho^i(x,y)$

(d) $\tilde{g}^{dense}(x,y)$ (e) $\rho^{fdense}(x,y)$ (f) $u^{dense}(x,y)$

(g) $\tilde{g}(x,y)$ (h) $\rho^f(x,y)$ (i) $u(x,y)$

(j) $\Delta\tilde{g}(x,y)$ (k) $\Delta\rho^f(x,y)$ (l) $\Delta u(x,y)$

Figure 8: Analysis of 1D-MDIC efficiency, comparison between a "dense" and an interpolated approach: first row the initial configuration in terms of real image (a), the model image (b) and the initial residual (c); second to fourth row: respectively the results of "dense" approach ((d) to (f)), the results of interpolated approach ((g) to (i)) and their differences ((j) to (l)), in terms of final deformed image $\tilde{g}$, final residuals ρ^f and displacement field u. The residual and difference maps (except for the displacement field) are normalized with respect to the image dynamic range and refer to the left colorbar, while the displacement fields refer to the right colorbar. The final disposition of yarn columns is shown in green, while their initial configuration is in red.

4.3. 2D-MDIC formulation

The 2D formulation for the MDIC algorithm builds on top of the chosen 2D extension of 1D-MDIC (interpolated version). Indeed, the calculations are not performed at every vertical or horizontal line of the 2D images, but rather a FE formulation is used for interpolating the obtained displacement field. As such, a structured 2D FE mesh with nodal positions corresponding to the yarn crossing points (identified in the 1D signals as detailed in section 3.3).

Also, just as in the case for 1D-MDIC, the parametric formulation of deformed image $g(x, y)$ embeds the kinematics as offsets to the center of the Gaussian profiles. These are u_i^x and u_i^y, corresponding to the nodal displacements of the horizontal and vertical Gaussian profiles respectively, whose index $i \in [1, n_{cweft} n_{cwarp}]$ sweeps all yarn columns crossing points. Let us stress that a horizontal profile corresponds to a Gaussian signal oriented along the x axis, while a vertical profile corresponds to a signal oriented along the y axis. As such, the corrected image is defined as

$$\tilde{g}(x, y) = c_0 + \sum_{l=1}^{n_{cweft}} \mathbb{G}(x;\ \alpha_l, x_l^0 + u_l^x(y), \omega) + \sum_{m=1}^{n_{cwarp}} \mathbb{G}(y;\ \beta_m, y_m^0 + u_m^y(x), \omega) \tag{23}$$

where the displacement fields $u_l^x(y)$ and $u_m^y(x)$ can vary along the cross direction of the Gaussian profiles (vertical stripes, here corresponding to weft yarn columns, are horizontally deformed while horizontal stripes, the warps, are vertically deformed).

The implementation details for solving this 2D MDIC formulation are given in Appendix A and, for convenience, the function `2D_MDIC`($f(x, y)$, $g(x, y)$) is defined.

As done previously, this 2D MDIC formulation will be compared with a multiple 1D MDIC strategy (along each direction). The former case implies only calculation, while the latter requires blurring operations (to obtain $I_{z,warp}(x, y)$ and $I_{z,weft}(x, y)$) and multiple 1D MDIC calculations at the yarn columns positions (FE mesh lines). The chosen reference image is the z-averaged image of the tomographic volume, *i.e.*, $I_z(x, y)$. The obtained vertical and horizontal displacement fields, shown in figure 9, are very similar. Yet, the elapsed time for the 2D MDIC calculation is 20 times that of the multiple 1D MDIC calculations (2 seconds vs 0.2 seconds, respectively). Thus, in the next paragraphs, the solution only the 1D MDIC algorithm will be taken for performing the correction of yarn distortions (*i.e.*, `1D_MDIC`).

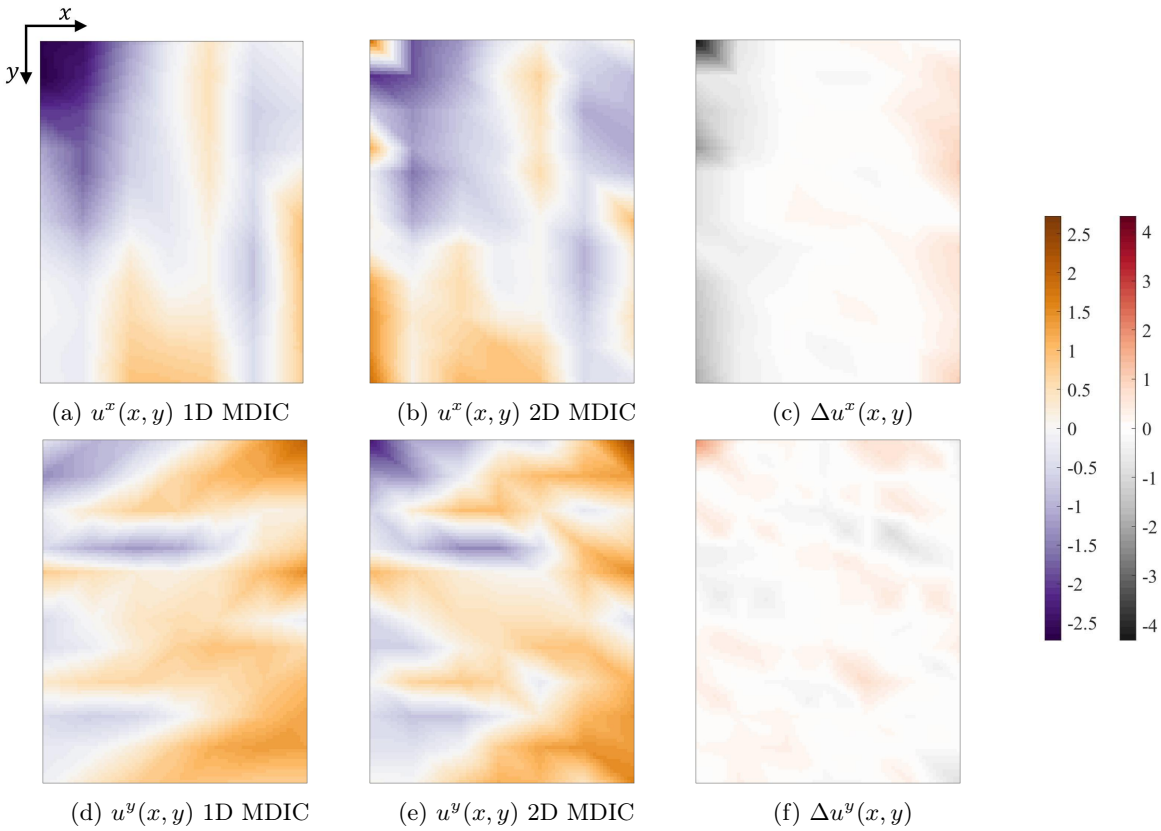

(a) $u^x(x, y)$ 1D MDIC (b) $u^x(x, y)$ 2D MDIC (c) $\Delta u^x(x, y)$

(d) $u^y(x, y)$ 1D MDIC (e) $u^y(x, y)$ 2D MDIC (f) $\Delta u^y(x, y)$

Figure 9: Comparison of sought displacement fields obtained using a series of interpolated 1D MDIC registrations ((a) and (d)) vs a 2D MDIC formulation ((b) and (e)) and their differences ((c) and (f)): the top row describes the registration directed along x (correction of weft yarns) while the bottom row describes the registration directed along y (correction of warp yarns). Displacement fields refer to the left colorbar, while difference maps refer to the right colorbar.

4.4. MDIC algorithm - 2D correction

The whole MDIC iterative procedure aims to analyze an input image $I'_z(x,y)$ for identifying the optimal displacement field $u(x,y)$ that best aligns the textile. For convenience, let us first define some helper functions: GATHER($u^x(x,y)$, $u^y(x,y)$), which combines two 2D displacement fields, and DEFORM2($I_z(x,y)$, $u(x,y)$), that applies the displacement field given by GATHER onto the 2D image to realign. In particular, the DEFORM2 function is as follows:

$$\tilde{I}_z(x,y) = I_z(x + u^x(x,y), y + u^y(x,y)) \tag{24}$$

Algorithm 1: Complete MDIC algorithm - 2D correction

$I'_z(x,y) \leftarrow$ Z_MEAN($V_{ct}(x,y,z)$) // section 3.1
$u(x,y) \leftarrow 0$
do
  $I_{z,warp}(x,y)$, $I_{z,weft}(x,y) \leftarrow$ GAUSSIAN_BLUR($I'_z(x,y)$) // section 3.1
  $I^M(x,y)$, $I^M_{warp}(x,y)$, $I^M_{weft}(x,y) \leftarrow$ GET_MODEL($I'_z(x,y)$) // sections 3.2 and 3.3
  if use 1D variant
    $u^x(x,y) \leftarrow$ 1D_MDIC($I_{z,weft}(x,y)$, $I^M_{weft}(x,y)$) // section 4.2
    $u^y(x,y) \leftarrow$ 1D_MDIC($I_{z,warp}(x,y)$, $I^M_{warp}(x,y)$)
  else if use 2D variant
    $u^x(x,y)$, $u^y(x,y) \leftarrow$ 2D_MDIC($I'_z(x,y)$, $I^M(x,y)$) // section 4.3
  end
  $u(x,y) \leftarrow u(x,y) +$ GATHER($u^x(x,y)$, $u^y(x,y)$) $+ u^{eq}(x,y)$
  $\tilde{I}_z(x,y) \leftarrow$ DEFORM2($I_z(x,y)$, $u(x,y)$)
  $I'_z(x,y) \leftarrow \tilde{I}_z(x,y)$
while RMS($I'_z(x,y)$, $\tilde{I}_z(x,y)$) $< \epsilon$

A great MDIC iteration is detailed within the **do**/**while** loop in algorithm 1. Here, both 1D or 2D variants of MDIC registrations can be used in order to obtain the displacement fields $u^x(x,y)$ and $u^y(x,y)$. Note that when the 1D method is employed, the partial images $I_{z,weft}(x,y)$ and $I_{z,warp}(x,y)$ and their corresponding models are employed (*i.e.*, $I^M_{weft}(x,y)$ and $I^M_{warp}(x,y)$). For the 2D method, the image $I'_z(x,y)$ and the image model $I^M(x,y)$ are used.

Next, it is important to note that both model creation and model identification steps are always applied on the current best-aligned image $I'_z(x,y) \leftarrow \tilde{I}_z(x,y)$. They follow the procedure detailed in section 3 and are summarized by the functions GAUSSIAN_BLUR and GET_MODEL used in algorithm 1. Moreover, as each of these 1D_MDIC and 2D_MDIC are also iterative procedures, they have their own convergence criteria.

Finally, a 2D displacement field $u^{eq}(x,y)$ (also expressed using FE shape functions) can be added

to $u(x, y)$ for imposing a supplementary textile assumption: yarn columns are equally spaced. The nodal values of this constant additional displacement field are

$$u_l^{x,eq} = x_l - (x_1 + (l-1)\lambda_x) \tag{25}$$

$$u_m^{y,eq} = y_m - (y_1 + (m-1)\lambda_y) \tag{26}$$

and can be computed just once immediately after the identification of the model. Note that at the end of every great iteration, this additional displacement field is just added to the one obtained by the correlations previously described.

When using such an iterative method, the correction of the textile image has been reached in three great iterations in less than 4 seconds. The structured mesh and deformed mesh superposed on their corresponding 2D images are shown in figure 10. During the process, nodal positions in the model image (see figure 10a) move towards the real textile (see figure 10b). The opposite of the displacement field re-aligns the yarn columns to a more regular configuration which completely matches the structural nodal positions of the model image, as shown in figure 10c. Finally, the addition of equal spacing between yarn columns translates the nodes to a disposition with a perfectly constant distance in both directions (see figure 10d). However, one can see that most of the in-plane distortions are well corrected when taking into account either with or without yarn column equal spacing. So, the simplest case (including equal spacing assumption) could be taken into account for easing the realignment treatment of the tomography.

4.5. MDIC algorithm - 3D correction

During the forming process, the yarn columns within 3D woven textiles are most of the time bent due to the shearing. These kinds of in-plane yarn distortions could be observed from figure 2 on few yarn columns. In real parts, this phenomenon is even more pronounced. This leads to the fact that the previous 2D method based on the z-averaging is no longer suitable.

However, over small distances along z, the same methodology is expected to be applicable. Thus, it is proposed to introduce a Gaussian blurring operation along the z axis to be applied on the tomographic volume $V_{ct}(x, yz)$, as a first transformation. This is achieved with a kernel $G(0, 0, l_z)$ of "zero-width" on the x and y axes, and l_z along the z axis. Using a large value of l_z (such as the entire thickness of the sample) leads to the previous 2D approach, since the z-blurring will become z-averaging. However, a lower limit on l_z is the average distance λ_z between two consecutive textile

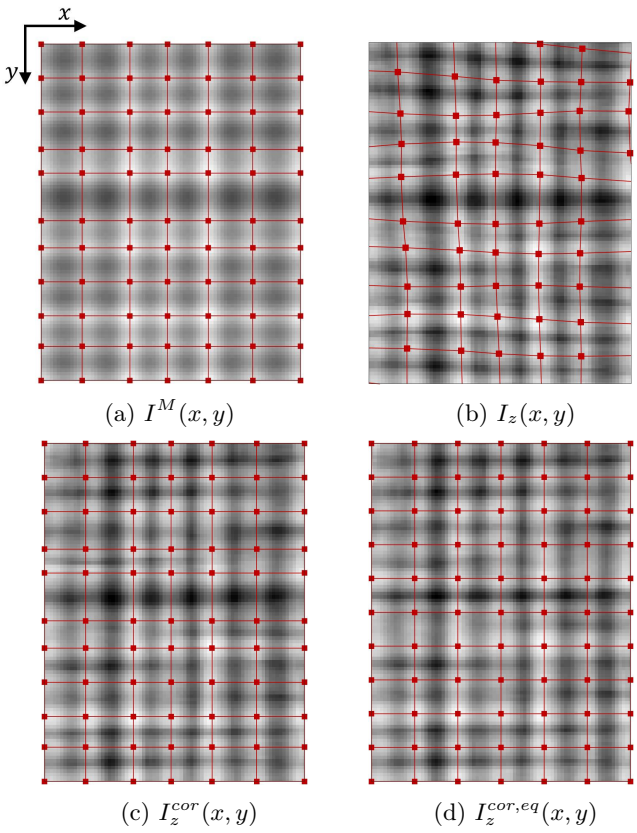

(a) $I^M(x, y)$ (b) $I_z(x, y)$

(c) $I_z^{cor}(x, y)$ (d) $I_z^{cor,eq}(x, y)$

Figure 10: Correction of the woven textile using the procedure of algorithm 1: (a) represents the model with a structured mesh built upon, (b) shows the deformed mesh at the end of MDIC correlation following the distorted paths of the real textile image, while (c) and (d) display the corrected disposition of yarn columns, respectively without and with equally spacing assumption, which perfectly match the undeformed mesh nodal positions.

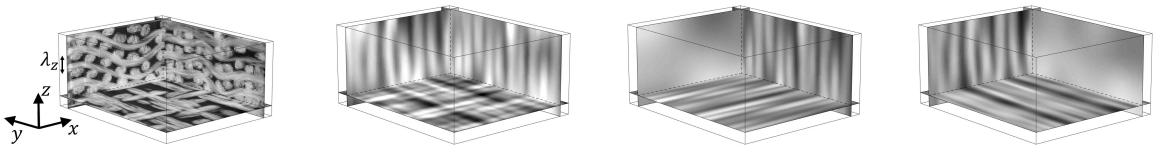

(a) $V_{ct}(x, y, z)$ (b) $V_z(x, y, z)$ (c) $V_{warp}(x, y, z)$ (d) $V_{weft}(x, y, z)$

Figure 11: 3D Gaussian blurring: (a) raw volume (in red the mean inter-yarn distance along the thickness λ_z); (b), (c) and (d) the blurred volumes showing respectively the evolution of the yarn crossing points along the thickness, just the warp surfaces, and just the weft surfaces.

layers (*e.g.*, see figure 11a). The appropriate value for l_z should be such that the distortion of the textile along z does not lead to an overlap of two yarn columns over this distance. In the following, the minimum value $l_z = \lambda_z$ is chosen to show that such an extreme choice, *i.e.*, the most tolerant to large textile distortion, works nicely.

For example, $\lambda_z = 10$ in the dry textile sample. Thus, the z-blurring transforms every initial warp and weft yarn column as smoothly varying along the z axis, as shown in the resulting volume $V_z(x, y, z)$ figure 11b.

Afterwards, in order to separate warp yarns from weft ones, two further Gaussian blurring operations are performed directly on the volume $V_z(x, y, z)$, similarly to the process detailed in section 3.1. Figures 11c and 11d, representing respectively $V_{warp}(x, y, z)$ and $V_{weft}(x, y, z)$ volumes after the z-blurring operation, show the yarn columns as vertical layered structures which are not entirely straight.

The series of Gaussian blurring operations are synthesized as

$$V_z(x, y, z) = G(0, 0, \lambda_z) \circledast V_{ct}(x, y, z) \tag{27}$$

$$V_{warp}(x, y, z) = G(\lambda_x, 0, 0) \circledast V_z(x, y, z) = G(\lambda_x, 0, \lambda_z) \circledast V_{ct}(x, y, z) \tag{28}$$

$$V_{weft}(x, y, z) = G(0, \lambda_y, 0) \circledast V_z(x, y, z) = G(0, \lambda_y, \lambda_z) \circledast V_{ct}(x, y, z) \tag{29}$$

It can be noted that $I_z(x, y)$, $I_{z,warp}(x, y)$ and $I_{z,weft}(x, y)$ can be retrieved just by applying `Z_MEAN` function respectively to $V_z(x, y, z)$, $V_{warp}(x, y, z)$ and $V_{weft}(x, y, z)$.

Let us define the helper function `PREPROCESS` which incorporates both the function `Z_MEAN` and the three-dimensional version of function `GAUSSIAN_BLUR`, for computing $I'_z(x, y)$, $V_z(x, y, z)$, $V_{warp}(x, y, z)$, $V_{weft}(x, y, z)$ from input volume $V'_{ct}(x, y, z)$. Here, for keeping coherence with notations, the z-averaged image I_z is labeled with $'$ for underlying, similarly to what is illustrated in the 2D correction algorithm,

its varying nature in the algorithm (it is computed from the updated volume V'_{ct}). Moreover, let the volume transformation

$$\tilde{V}_{ct}(x,y,z) = V_{ct}(x + u^x(x,y,z), y + u^y(x,y,z), z) \tag{30}$$

be represented by the function DEFORM3($V_{ct}(x,y,z)$, $u(x,y,z)$) applied onto the initial volume. Note that this transformation, although performed in 3D, respects the two-dimensional kinematics of the problem, described by displacement fields orthogonal to each mean yarn orientation.

The three-dimensional version of the procedure reported in algorithm 2 has the purpose of finding, at each great iteration, the displacement field that best aligns an updated volume $V'_{ct}(x,y,z)$ with its ideal modeling representation, also in this case described by the model image $I^M(x,y)$ or by its one-dimensional versions $I^M_{warp}(x,y)$, $I^M_{weft}(x,y)$, computed as in sections 3.2 and 3.3. Again, it is important to underline that all PREPROCESSING and GET_MODEL steps are always applied on the current aligned volume $V'_{ct}(x,y,z) \leftarrow \tilde{V}_{ct}(x,y,z)$. This procedure is repeated until a convergence criterion based on the RMS($V'_{ct}(x,y,z)$, $\tilde{V}_{ct}(x,y,z)$) is fulfilled.

The 3D displacement field can be estimated by multiple uses of the 2D_MDIC algorithm (or its one-dimensional version 1D_MDIC) for all slices z_k belonging to the blurred volume $V_z(x,y,z)$ (or the uncoupled versions $V_{warp}(x,y,z)$, $V_{weft}(x,y,z)$) with the corresponding model image. In concordance with the two-dimensional use of 1D_MDIC, the choice of computing as many z-slices as the thickness size is permitted. However, for improving the computational time, further simplification can take place and subsequent calculations are performed just on a set of chosen z-slices. Indeed, a similar reasoning to that in sections 4.2 and 4.3 is used here: to benefit from the regularization and continuity provided by FE interpolation. As such, instead of analyzing all possible z-slices, only those corresponding to the textile layers are chosen (gathered into z_{chosen}). Naturally, a single 3D structured FE mesh can be built with nodes placed at every yarn column mean crossing points (on x and y) and separated by a distance of λ_z (on z).

These calculations are illustrated in sections 4.2 and 4.3 and are detailed within the **forall** loop in algorithm 2 and highlighted in the diagram in figure 12. It is possible to note that the main difference with the simple 2D correction algorithm is that here the identified model image $I^M(x,y)$ is correlated with each z-slice of $V_z(x,y,z)$ and not directly with $I'_z(x,y)$.

In the following section, the results obtained with the 3D correction from algorithm 2 of both a woven textile and an injected woven composite will be illustrated. Let us recall that given the more

Algorithm 2: Complete MDIC algorithm - 3D correction

$V'_{ct}(x,y,z) \leftarrow V_{ct}(x,y,z)$
$u(x,y,z) \leftarrow 0$
do
  $I'_z(x,y)$, $V_z(x,y,z)$, $V_{warp}(x,y,z)$, $V_{weft}(x,y,z) \leftarrow$ PREPROCESS$(V'_{ct}(x,y,z))$
  $I^M(x,y)$, $I^M_{warp}(x,y)$, $I^M_{weft}(x,y) \leftarrow$ GET_MODEL$(I'_z(x,y))$ // sections 3.2 and 3.3
  for all $z_k \in z_{chosen}$
    if use 1D variant
      $u^x(x,y) \leftarrow$ 1D_MDIC$(V_{weft}(x,y,z_k), I^M_{weft}(x,y))$ // section 4.2
      $u^y(x,y) \leftarrow$ 1D_MDIC$(V_{warp}(x,y,z_k), I^M_{warp}(x,y))$
    else if use 2D variant
      $u^x(x,y), u^y(x,y) \leftarrow$ 2D_MDIC$(V_z(x,y,z_k), I^M(x,y))$ // section 4.3
    end
    $u(x,y,z_k) \leftarrow u(x,y,z_k) +$ GATHER$(u^x(x,y), u^y(x,y)) + u^{eq}(x,y)$
  end
  $\tilde{V}_{ct}(x,y,z) \leftarrow$ DEFORM3$(V_{ct}(x,y,z), u(x,y,z))$
  $V'_{ct}(x,y,z) \leftarrow \tilde{V}_{ct}(x,y,z)$
while RMS$(V'_{ct}(x,y,z), \tilde{V}_{ct}(x,y,z)) < \epsilon$

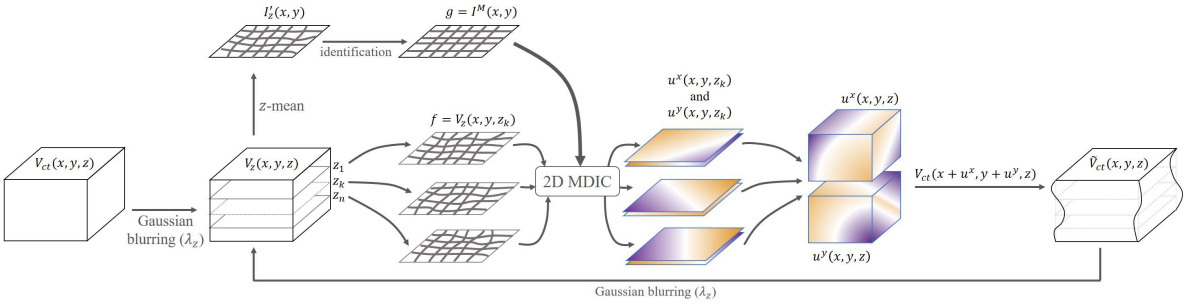

Figure 12: Diagram of MDIC algorithm for the complete textile volume correction.

regular disposition of yarn columns, only the case of equally spaced columns is taken into account.

5. Results

This section presents the results of the MDIC algorithm on both samples: a 3D woven preform and a woven composite sample. The MDIC formulation is the one that benefits from interpolation (from 3D to 2D and from 2D to 1D), hence it uses multiple 1D MDIC registrations. Moreover, the equal spacing variant is also enforced.

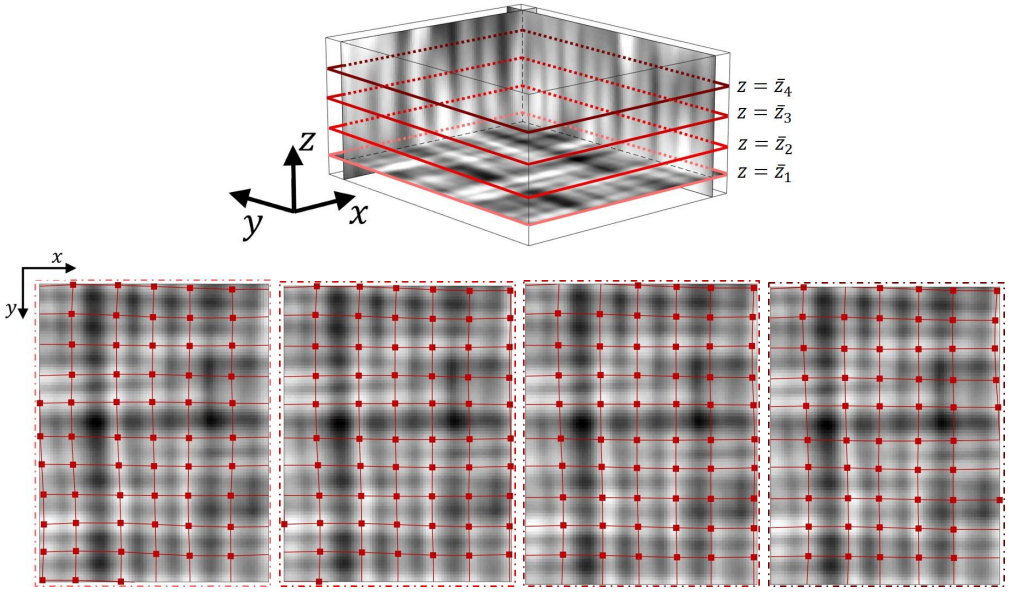

Figure 13: Illustration of the 3D correction showing the deformed mesh of four z-slices of the complete textile volume. The slices are extracted from the volume as shown on the top figure, whereas the bottom line displays the four slices $z = \bar{z}_1$ to $\bar{z}_4$ from left to right.

5.1. 3D woven preform sample

The results of the MDIC for the 3D woven textile corrections show both yarn columns orientations in a perfectly straight and orthogonal disposition. Moreover, the assumption of equally spaced columns forces this yarn disposition to be much more regular.

A total number of six greater iterations are enough for a full correction of the volume image, which has been obtained with a total elapsed time of 20 seconds (each great iteration is performed in no more than 3.5 seconds). Given that all calculations are computed in the coarsened volume, the found displacement at this scale can be interpolated so that a finer correction can be provided also for the original volume. It should be noted that its intensity has been multiplied by 16, which represents the in-plane scale factor between the original and the coarse volumes.

Figure 13 illustrates the 3D correction of the preform with the mesh plotted in red on top of the yarns, for four different slices equally distributed in the sample height.

Figures 14 and 15 show three equally-spaced vertical slices of the tomography directed both as the x-z plane (representing weft yarn cross-sections) and the y-z plane (representing warp yarn cross-sections). For the same chosen slice it is shown the initial, the final configuration, and the corresponding difference map. As it can be observed, after the correction the columns are more vertical and present a more regular disposition. Moreover, as shown in the difference maps, most of the displacement

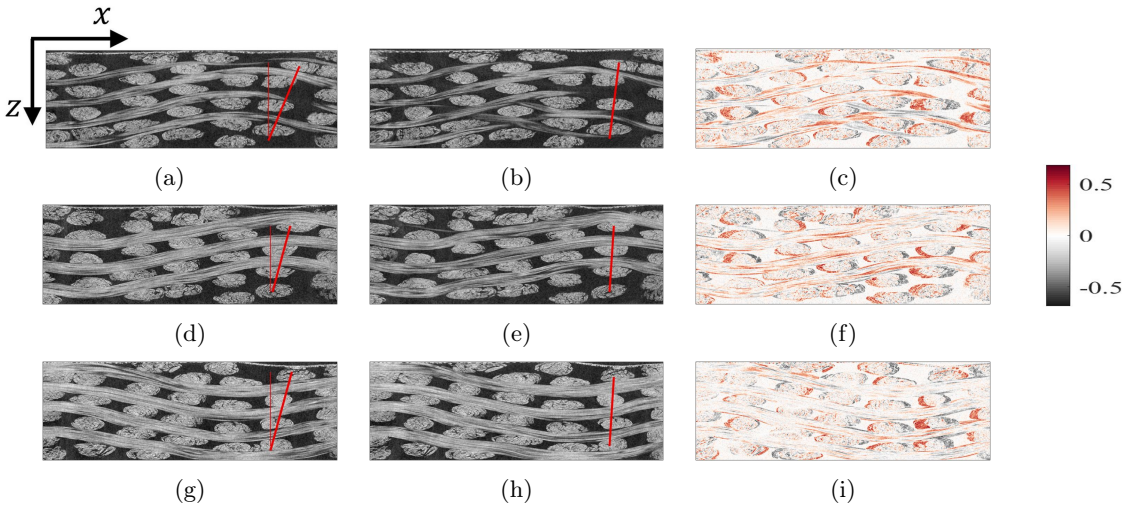

Figure 14: Correction of weft yarn columns of a 3D woven textile at different x-z slices: (from top to bottom $y = 444$, $y = 888$ and $y = 1332$ pixel) first column initial, second column corrected (a thick red line corresponding to a yarn column highlights the performed correction), third column their difference maps normalized by the image dynamics.

occurred along the weft direction, whilst the warp yarns remain almost untouched. This is described by a stronger alternation of positive and negative values of the difference map in the x-z slices around the yarn cross-sections, while, along the y-z direction, the elongated structures representing the cross yarns show a high absolute value. This can be easily explained by the fact that the direction of the warp is more controllable and denser than the weft.

However, it should be noted that given the fact that the method was applied at a coarser scale (focusing only on the change in position of the yarn neutral fiber), the displacements cause some non-physical distortions of the cross-sections.

Moreover, similar results are exploitable when looking at the volume images of the initial and final configurations, reported in figure 16. Two vertical slices of the volumes are properly chosen to help read these transformations: if, before the correction, yarn columns corresponded rather to irregular surfaces and yarns continuously appeared and disappeared on these slices, after the correction the regularity mean that the displaced yarns are clearly visible throughout their entire length.

Finally, z-averaging of the volume has been computed for observing all the transformations that occurred in the textile within a single 2D image. As shown in figure 17, yarn columns are much more aligned, and the structure formed by the crossing points presents constant distances in both directions. In addition, it is noteworthy how the intensity of the image at various points has changed due to the

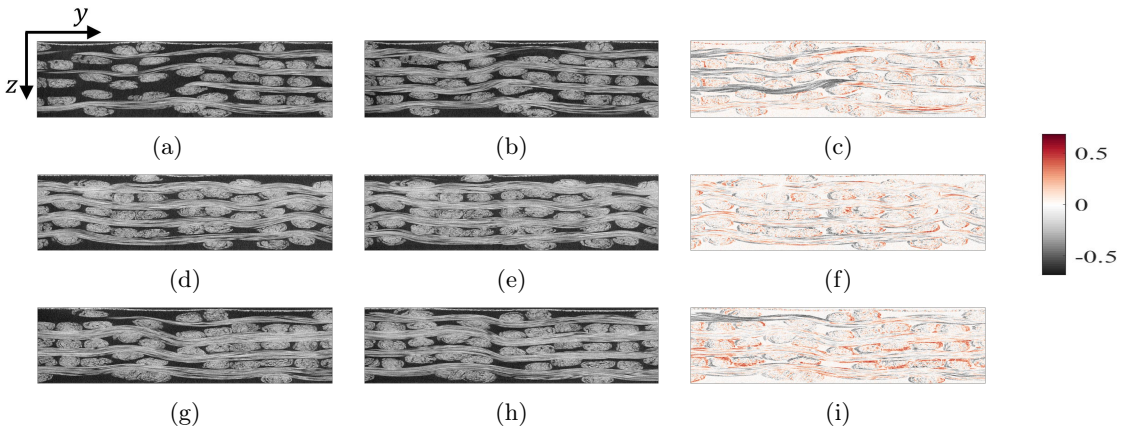

Figure 15: Correction of warp yarn columns of a 3D woven textile at different y-z slices: (from top to bottom $x = 368$, $x = 736$ and $x = 1104$ pixel) first column initial, second column corrected, third column their difference maps normalized by the image dynamics.

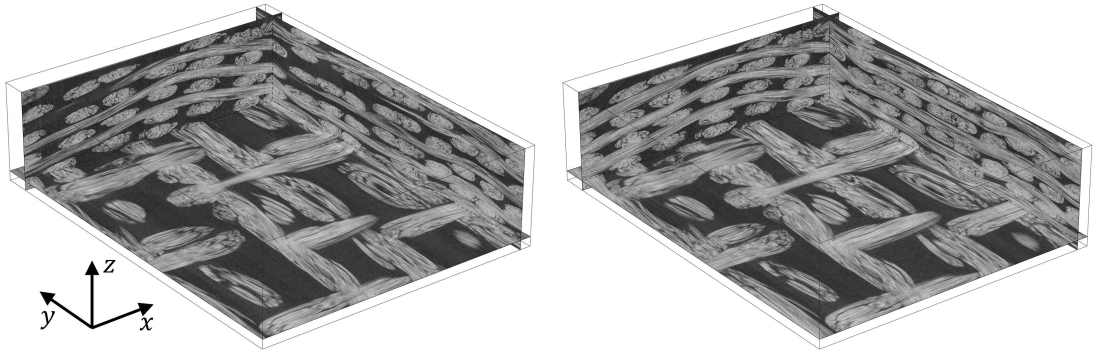

(a) V_{ct} (b) V_{ct}^{cor}

Figure 16: (a) Initial and (b) corrected volumes of the 3D woven textile.

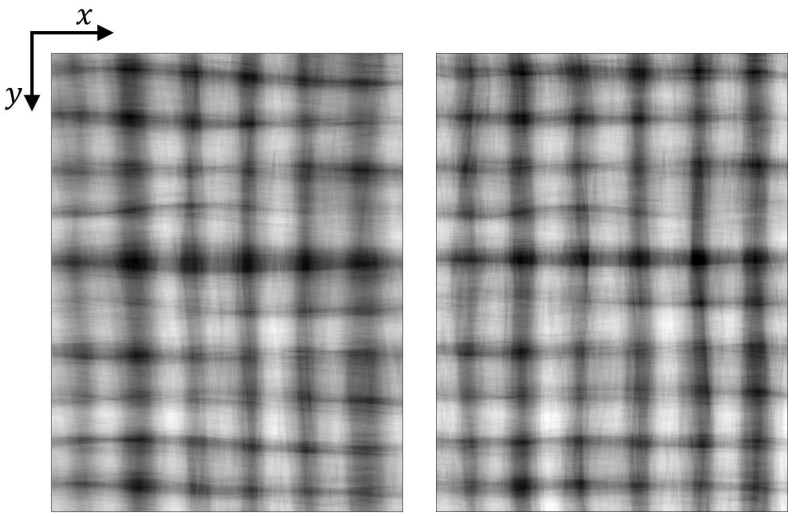

(a) I_z (b) z-mean projection of V_{ct}^{cor}

Figure 17: z-averaged image of a 3D woven textile: (a) initial and (b) corrected configurations.

3D correction. This is due to having "moved" the yarns back to a correct position belonging to vertical columns; thereby, the integral of the gray level in the volume (*i.e.*, matter density), is affected by this "physical" change.

5.2. 3D woven composite sample

While the previous sections used a dry sample (*i.e.*, only the textile reinforcement is present), here a "complete" composite is explored (injected with an epoxy resin). Now the specimen images use inj subscript for referring to an injected preform (*i.e.*, a woven composite) sample.

For this volume, $\lambda_x = 23$, $\lambda_y = 15$, and $\lambda_z = 8$ were estimated as the distances between weft columns, warp columns, and thickness layers, respectively. Given the more regular textile structure, the results of the full 3D alignment are obtained with just one great iteration, computed in 8.5 seconds (note the higher number of yarns, but however the use of just one great iteration).

Figures 18 and 19 show three equally-spaced vertical slices of the volume, directed both along the warp and weft directions, in their initial and final configurations. As well, the third column of each figure illustrates the relative difference map. It is even more evident in this case, that the most of textile deformations occurred along the weft direction, while the warp yarn columns remain very similar to the initial configuration, which already presented a regular pattern. Indeed, strong variations of the gray level around the weft yarn cross-sections for the x-z slices are accompanied by those within inter-cross-section spaces for the y-z slices.

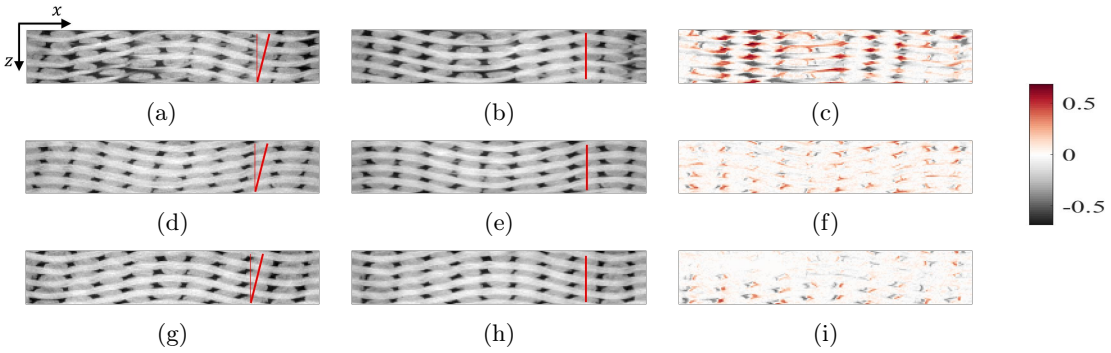

Figure 18: Correction of weft yarn columns of a 3D woven composite at different x-z slices: (from top to bottom $y = 64$, $y = 128$ and $y = 192$ pixel) first column initial, second column corrected (a thick red line corresponding to a yarn column highlights the performed correction), third column their difference maps normalized by the image dynamics.

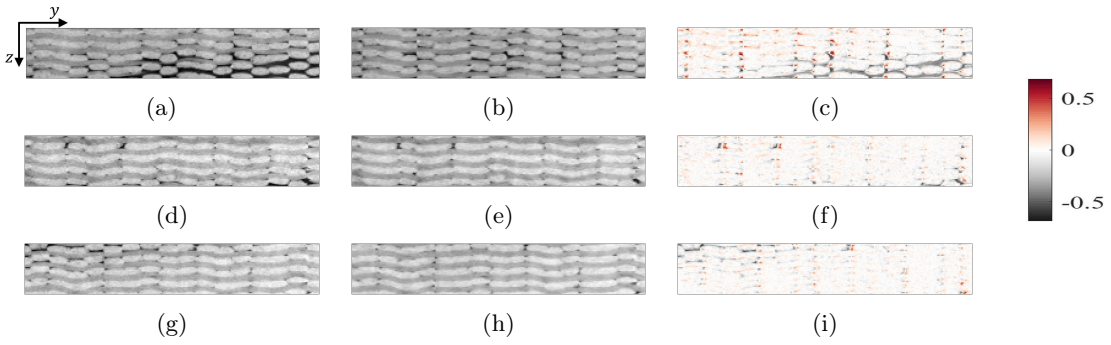

Figure 19: Correction of warp yarn columns of a 3D woven composite at different y-z slices: (from top to bottom $x = 64$, $x = 128$ and $x = 192$ pixel) first column initial, second column corrected, third column their difference maps normalized by the image dynamics.

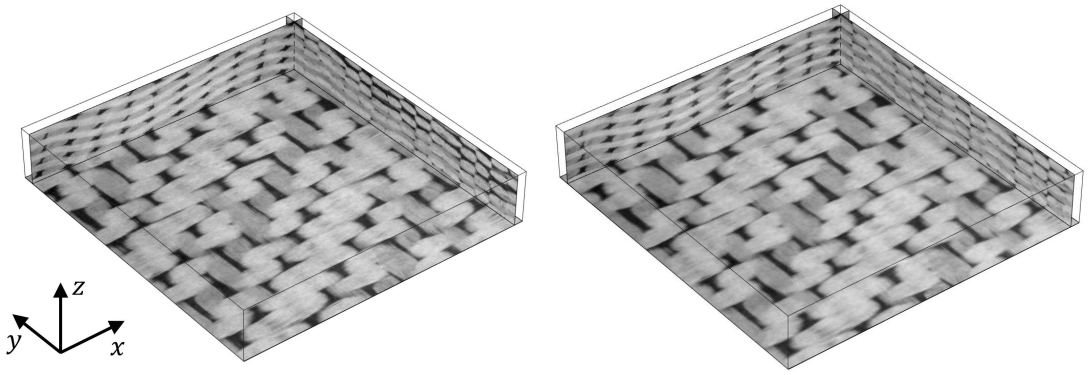

(a) $V_{ct,inj}$ (b) $V^{cor}_{ct,inj}$

Figure 20: (a) Initial and (b) corrected volumes of the 3D woven composite.

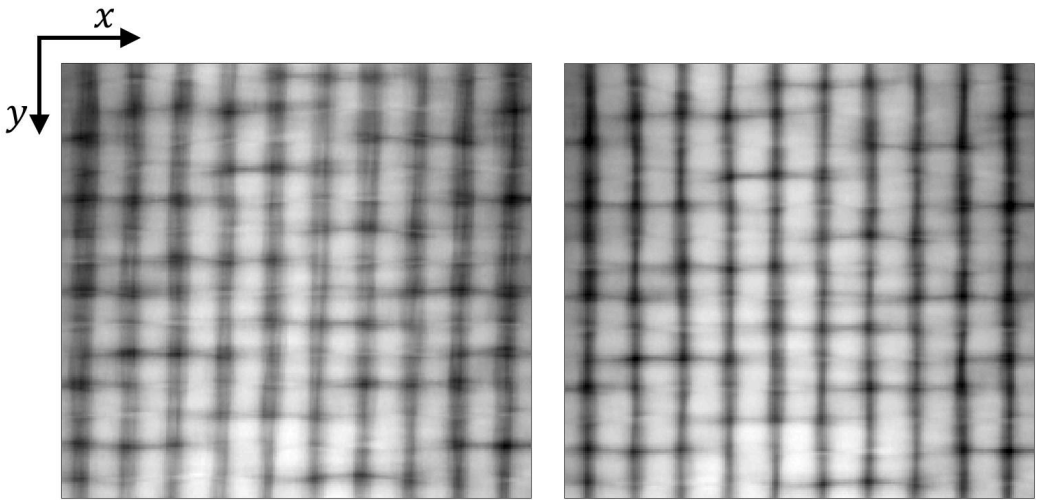

(a) $I_{z,inj}$ (b) z-mean projection of $V^{cor}_{ct,inj}$

Figure 21: z-averaged image of a 3D woven composite: (a) initial and (b) corrected configurations.

When looking at the whole volumes shown in figure 20, not only yarn columns are now aligned with the x and y axes (and orthogonal between themselves), but also the yarns in each column remain now properly in the same vertical thick plane (respectively x-z for warp and y-z for weft columns). Moreover, the global composite deformation suggests that shearing of the weft structure directed along the thickness occurred during the manufacturing process. This is confirmed also when z-mean projection images (see figure 21), which decodes this deformation of weft columns to an increase of their z-mean gray levels.

6. Conclusions

In this study, a novel use of Digital Image Correlation has been proposed for converting the tomography of a woven textile to a more ideal configuration, in which the yarn columns are perfectly straight, vertical and orthogonal. It is noteworthy that the proposed method could be seen as a pre-processing step to image segmentation procedures or to ease the visual inspection performed by operators since the yarn paths and yarn column deformations could be significant during the composite material manufacturing.

This objective has been accomplished by registering the tomography with a parametric model of the textile, which stemmed directly from the observed weaving (*e.g.*, yarn sizes, column spacing, weaving pattern). Moreover, the registration process is based on only one reference image, from which the "deformed" state is constructed. This novel idea leads to the MDIC method.

Besides, the construction of the model provides more freedom in the DIC formulation, as the elements included in the model are easily adapted to the DIC minimization problem. Also, since the goal of this study is to realign the real textile image, the latter is back-corrected with the opposite of the displacement field obtained by the registration of the model image onto the real one.

The MDIC method has been presented as multiple 2D problems or as multiple 1D problems. In the former case, the algorithm tackles the misalignment of warp and weft columns simultaneously. In the latter case, each orientation is handled separately. Moreover, the 1D version of the MDIC formulation is much faster and provides better-conditioned results compared to the 2D one.

Furthermore, it has been shown that if the yarn columns of the textile are sufficiently straight, a correction of the z-mean projection of the tomographic volume can be directly performed. However, for more distorted yarn columns along the thickness, the correction should be carried out by registering the same model throughout a given number of z-slices.

The complete correction method has been applied both on a woven textile and a composite tomographic volume for re-aligning yarn column distortions.

Furthermore, the displacement required for aligning the weft columns was found to be greater than the one for warp columns (in both specimens). Moreover, since the composite part is more compact than the textile sample, all columns seem to have a homogeneous shearing along the thickness direction. As such, it is worth noting that this method not only provides a successful correction of yarn column distortions but also allows quantitative and qualitative analysis of all textile deformations that occurred

during the manufacturing process (*e.g.*, bending, shearing).

As a perspective, the presented procedure could be extended to deform ideal textiles performed by some Textile Geometry Pre-processors such as TexGen [27] or WiseTex [28] in order to generate from them more realistic textile models suitable for mechanical FE simulations. This would presumably open the methodology to more complex textile architectures. A further extension of this work could be to address the through-the-thickness displacement field, after the (x, y) alignment.

7. Acknowledgments

Marcello Rubino acknowledges the support of a PhD grant N° 2019/1662 from ANRT and Safran Aircraft Engines. The authors thank the anonymous reviewers for their constructive comments.

Appendix A. Derivation details for 2D MDIC

It is important to note that, while the initial position of the Gaussian profiles remains constant for all "lines" orthogonal to the orientation of the profiles, the associated displacements do not. As such, when initially $u_l^x(y) = 0$ and $u_m^y(x) = 0$, the obtained image is essentially composed of perfectly vertical and horizontal stripes (weft and warp). However, as these values evolve, the vertical stripes are horizontally deformed, and the horizontal stripes are vertically deformed. Crucially, this is performed on the parametric function $\tilde{g}(x, y)$, which allows for the non-conservation of gray levels evoked beforehand.

As such, the displacements $u_l^x(y)$ and $u_m^y(x)$ are also expressed using a 1D FE formulation

$$u_l^x(y) = \sum_{m=1}^{n_{cwarp}} u_{l,m}^x \cdot \psi_{1D_m}(y) \tag{A.1}$$

$$u_m^y(x) = \sum_{l=1}^{n_{cweft}} u_{m,l}^y \cdot \psi_{1D_l}(x) \tag{A.2}$$

with $u_{l,m}^x$ labeling the displacement of the horizontal profile l at the vertical position of node m, while $u_{m,l}^y$ identifies the displacement of the vertical profile m, at horizontal position of node l. It may be worth noting that, given that the series of Gaussian profiles naturally provide the continuity along the signal direction, such interpolation is only required in directions orthogonal to the Gaussian profile. As such, this formulation represents something unusual for DIC, for which rather a classical two-dimensional FE mesh is used for computing the algorithm. Let us call u_i^x and u_i^y the nodal values

(counted now as the total degrees of freedom of the MDIC problem), which are gathered into a vector $\{p\}$. This vector of parameters is of length $2n_{cweft}n_{cwarp}$ ($l \in [1, n_{cweft}]$ and $m \in [1, n_{cwarp}]$, or equivalently $i \in [1, n_{cweft}n_{cwarp}]$).

The solution to the linear approximation of the problem is iteratively solved with the linear system:

$$[M]\{\delta p\} = \{b\} \tag{A.3}$$

with

$$[M] = \begin{bmatrix} M^{xx} & M^{xy} \\ M^{yx} & M^{yy} \end{bmatrix} \tag{A.4}$$

$$\{b\} = \begin{Bmatrix} b^x \\ b^y \end{Bmatrix} \tag{A.5}$$

because of the interaction between directions x and y, the sub-matrices and sub-vectors are then defined as:

$$M_{ij}^{xx} = \sum_{(x,y)\,\in\,\Omega} S_i^x(x,y) S_j^x(x,y) \tag{A.6}$$

$$M_{ij}^{xy} = \sum_{(x,y)\,\in\,\Omega} S_i^x(x,y) S_j^y(x,y) \tag{A.7}$$

$$M_{ij}^{yx} = \sum_{(x,y)\,\in\,\Omega} S_i^y(x,y) S_j^x(x,y) \tag{A.8}$$

$$M_{ij}^{yy} = \sum_{(x,y)\,\in\,\Omega} S_i^y(x,y) S_j^y(x,y) \tag{A.9}$$

$$b_i^x = \sum_{(x,y)\,\in\,\Omega} S_i^x(x,y) \rho(x,y) \tag{A.10}$$

$$b_i^y = \sum_{(x,y)\,\in\,\Omega} S_i^y(x,y) \rho(x,y) \tag{A.11}$$

The corresponding sensitivity fields are also differentiated with respect to directions x and y

$$
\begin{aligned}
S_i^x(x,y) &= \frac{\partial}{\partial u_i^x}\tilde{g}(x,y) \qquad (A.12)\\
&= \left[\frac{\partial}{\partial u_i^x}\mathbb{G}(x;\ \alpha_i, x_i^0 + u_i^x, \omega)\right]\psi_{1D_i}(y)\\
&= \left[\alpha_i \frac{(x - x_i^0 - u_i^x)}{\omega^2}\exp\left(-\frac{(x - x_i^0 - u_i^x)^2}{2\omega^2}\right)\right]\psi_{1D_i}(y)\\
S_i^y(x,y) &= \frac{\partial}{\partial u_i^y}\tilde{g}(x,y) \qquad (A.13)\\
&= \left[\frac{\partial}{\partial u_i^y}\mathbb{G}(y;\ \beta_i, y_i^0 + u_i^y, \omega)\right]\psi_{1D_i}(x)\\
&= \left[\beta_i \frac{(y - y_i^0 - u_i^y)}{\omega^2}\exp\left(-\frac{(y - y_i^0 - u_i^y)^2}{2\omega^2}\right)\right]\psi_{1D_i}(x)
\end{aligned}
$$

Finally, the parameters at iteration k are updated following:

$$\{p\}^{(k+1)} = \{p\}^{(k)} + \{\delta p\} \qquad (A.14)$$

References

[1] Safran, LEAP-1A, a new-generation engine for the A320neo family, https://www.safran-group.com/products-services/leap-1a-new-generation-engine-single-aisle-commercial-jets, 2022. Accessed: 2022-12-16.

[2] F. Desplentere, S. V. Lomov, D. L. Woerdeman, I. Verpoest, M. Wevers, A. Bogdanovich, Micro-ct characterization of variability in 3d textile architecture, Composites Science and Technology 65 (2005) 1920–1930.

[3] T. Gereke, C. Cherif, A review of numerical models for 3d woven composite reinforcements, Composite Structures 209 (2019) 60–66.

[4] N. Naouar, D. Vasiukov, C. H. Park, S. V. Lomov, P. Boisse, Meso-FE modelling of textile composites and X-ray tomography, Journal of Materials Science 55 (2020) 16969–16989.

[5] Y. Wielhorski, A. Mendoza, M. Rubino, S. Roux, Numerical modeling of 3d woven composite reinforcements: A review, Composites Part A Applied Science and Manufacturing 154 (2022) 106729.

[6] I. Straumit, S. V. Lomov, M. Wevers, Quantification of the internal structure and automatic generation of voxel models of textile composites from X-ray computed tomography data, Composites Part A: Applied Science and Manufacturing 69 (2015) 150–158.

[7] N. Naouar, E. Vidal-Sallé, J. Schneider, E. Maire, P. Boisse, 3D composite reinforcement meso F.E. analyses based on X-ray computed tomography, Composite Structures 132 (2015) 1094–1104.

[8] A. Mendoza, R. Trullo, Y. Wielhorski, Descriptive modeling of textiles using fe simulations and deep learning, Composites Science and Technology (2021) 108897.

[9] Y. Sinchuk, P. Kibleur, J. Aelterman, M. N. Boone, W. V. Paepegem, Geometrical and deep learning approaches for instance segmentation of cfrp fiber bundles in textile composites, Composite Structures 277 (2021) 114626.

[10] M. A. Ali, Q. Guan, R. Umer, W. J. Cantwell, T. Zhang, Deep learning based semantic segmentation of µct images for creating digital material twins of fibrous reinforcements, Composites Part A: Applied Science and Manufacturing 139 (2020) 106131.

[11] M. Ali, Q. Guan, R. Umer, W. J. Cantwell, T. Zhang, Efficient processing of µct images using deep learning tools for generating digital material twins of woven fabrics, Composites Science and Technology 217 (2022) 109091.

[12] S. Blusseau, Y. Wielhorski, Z. Haddad, S. Velasco-Forero, Instance segmentation of 3D woven fabric from tomography images by Deep Learning and morphological pseudo-labeling, Composites Part B 247 (2022) 110333.

[13] J. Bénézech, G. Couégnat, Variational segmentation of textile composite preforms from X-ray computed tomography, Composite Structures 230 (2019) 111496.

[14] V. Pidou-Brion, Y. Le Guilloux, Active yarn meshes for segmentation on x-ray computed tomography of textile composite materials at the mesoscopic scale, Composite Structures 281 (2022) 115084.

[15] M. Sutton, W. Wolters, W. Peters, W. Ranson, S. McNeill, Determination of displacements using an improved digital correlation method, Image and Vision Computing 1.3 (1983) 133–139.

[16] G. Besnard, F. Hild, S. Roux, Finite-element displacement fields analysis from digital images: Application to Portevin-Le Châtelier bands, The Journal of Strain Analysis for Engineering Design 43.8 (2008) 745–760.

[17] B. Bay, T. Smith, D. Fyhrie, M. Saad, Digital volume correlation: three-dimensional strain mapping using x-ray tomography, Experimental Mechanics 39 (1999) 217–226.

[18] S. Roux, F. Hild, P. Viot, D. Bernard, Three-dimensional image correlation from X-Ray computed tomography of solid foam, Composites Part A: Applied science and manufacturing 39 (2008) 1253–1265.

[19] A. Buljac, C. Jailin, A. Mendoza, J. Neggers, T. Taillandier-Thomas, A. Bouterf, B. Smaniotto, F. Hild, S. Roux, Digital volume correlation: Review of progress and challenges, Experimental Mechanics 58 (2018) 661–708.

[20] A. Mendoza, J. Schneider, E. Parra, S. Roux, The correlation framework: Bridging the gap between modeling and analysis for 3d woven composites, Composite Structures 229 (2019) 111468.

[21] A. Mendoza, J. Schneider, E. Parra, E. Obert, S. Roux, Differentiating 3D textile composites: A novel field of application for digital volume correlation, Composite Structures 208 (2018) 735–743.

[22] H. A. Bruck, S. R. McNeill, M. A. Sutton, W. H. Peters, Digital image correlation using Newton-Raphson method of partial differential correction, Experimental Mechanics 29.3 (1989) 261–267.

[23] H. Schreier, J.-J. Orteu, M. A. Sutton, Image Correlation for Shape, Motion and Deformation Measurements, Springer US, 2009.

[24] M. Grediac, F. Hild, Digital Image Correlation, Wiley & Sons, 2012.

[25] F. Hild, S. Roux, Digital image correlation: From displacement measurement to identification of elastic properties - a review, Strain 42(2) (2006) 69–80.

[26] Y. Sun, C. K. Wong, F. Su, J. H. L. Pang, Finite element formulation for a digital image correlation method, Applied Optics 44.34 (2005) 7357–7363.

[27] M. Sherburn, Geometric and Mechanical Modelling of Textiles, Ph.D. thesis, University of Nottingham, 2007.

[28] S. V. Lomov, A. V. Gusakov, G. Huysmans, A. Prodromou, I. Verpoest, Textile geometry preprocessor for meso-mechanical models of woven composites, Composites Science and Technology 60.11 (2000) 2083–2095.

List of Figures